Molecular Vision 2005; 11:569-81 <http://www.molvis.org/molvis/v11/a67/>
Received 06 June 2005 | Accepted 18 July 2005 | Published 27 July 2005

An ENU-induced mutation in *Rs1h* causes disruption of retinal structure and function

Monica M. Jablonski,[1,2] Claudia Dalke,[3] XiaoFei Wang,[1,2] Lu Lu,[2,4] Kenneth F. Manly,[2,4] Walter Pretsch,[5] Jack Favor,[5] Machelle T. Pardue,[6,7] Eugene M. Rinchik,[2] Robert W. Williams,[2,4] Daniel Goldowitz,[2,4] Jochen Graw[3]

(The first two authors contributed equally to this publication)

[1]Department of Ophthalmology and [4]Center of Genomics and Bioinformatics, University of Tennessee Health Science Center, Memphis, TN; [2]Tennessee Mouse Genome Consortium, Memphis, TN; [3]GSF-National Research Center for Environment & Health, Institute of Developmental Genetics and [5]Institute of Human Genetics, Neuherberg, Germany; [6]Veterans Administration Medical Center, Atlanta, GA; [7]Department of Ophthalmology, Emory University School of Medicine, Atlanta, GA

Purpose: The *44TNJ* mutant mouse was generated by the Tennessee Mouse Genome Consortium (TMGC) using an ENU-based mutagenesis screen to produce recessive mutations that affect the eye and brain. Herein we present its retinal phenotype and genetic basis.

Methods: Fourth generation offspring (G_4) and confirmed mutants were examined using slit lamp biomicroscopy, funduscopy, histology, immunohistochemistry, and electroretinography (ERG). *44TNJ* mutant mice were crossed to C3BLiA or DBA/2 mice for chromosomal mapping purposes. Linkage analysis by PCR-based microsatellite marker genotyping was used to identify the disease locus. The *Rs1h* cDNA and its genomic DNA were sequenced directly.

Results: The *44TNJ* pedigree was the first mutant pedigree identified by the ocular phenotyping domain of the TMGC. Examination of the fundus revealed numerous small and homogeneous intraretinal microflecks in the peripapillary region, which became courser and more irregular in the periphery. Males were typically more affected than females. Histology and immunohistochemistry revealed a disruption of the lamination of the retina, particularly at both margins of the outer nuclear layer, along with reduced calbindin immunostaining. ERG analyses revealed reduced amplitudes of both a-waves and b-waves. Linkage analysis mapped the *44TNJ* mutation to the X chromosome close to the marker *DXMit117*. Sequence analysis of the positional candidate gene *Rs1h* revealed a T->C exchange at the second base of intron 2 of the *Rs1h* gene.

Conclusions: We have generated and characterized a mutant mouse line that was produced using ENU-based mutagenesis. The *44TNJ* pedigree manifests with photoreceptor dysfunction and concurrent structural and functional aberrations at the post-receptoral level. Genetic analysis revealed a mutation in *Rs1h*, making this the first murine model of X-linked retinoschisis in which the gene is expressed.

X-linked retinoschisis (XLRS), the leading cause of juvenile macular degeneration affecting males, is caused by mutations in the *RS1* gene [1]. While hemizygous affected males present with microcystic-like changes of the macula and schisis of inner retinal layers, peripheral lesions also are present in about 50% of cases [2-5]. Visual impairment is typically manifest by age 5 in boys. The progression of the disease is slow and complications such as vitreal hemorrhage, choroidal sclerosis, and retinal detachment can occur later in life. Female obligate carriers are typically asymptomatic with no clinical features, although Kaplan et al. [6] found that heterozygous females can have full expression of the retinal disease. The expression of XLRS is variable even within families. Moreover, the severity of disease expression is not mutation specific [7].

Correspondence to: Monica M. Jablonski, PhD, Department of Ophthalmology, Hamilton Eye Institute, University of Tennessee Health Science Center, 930 Madison, Suite 731, Memphis, TN, 38163; Phone: (901) 448-7572; FAX: (901) 448-1299; email: mjablonski@utmem.edu

The human *RS1* gene consists of six exons that encode for a 224 amino acid protein of 24 kDa. The Rs1 protein is soluble, secretory, and forms disulfide-linked dimers and octamers [8]. The predicted protein sequence contains three domains: a signal sequence encoded by exons 1 and 2 (amino acids 1-23); an Rs1 domain encoded by exon 3 (amino acids 23-62); and a discoidin domain encoded by exons 4-6 (amino acids 63-219). In addition, there is a five amino acid segment present on the C-terminal side of the discoidin domain [9]. To date, over 133 different mutations in *RS1* have been documented [8] (see the RetinoschisisDB for details on specific mutations provided by the Retinoschisis Consortium). Most human mutations are in the discoidin domain with relatively few in signal or Rs1 domains, thereby suggesting that the discoidin domain and its putative role in cell adhesion are critical to the function of the protein [10-12].

Although the precise function of the protein remains incompletely understood, recent studies have determined that wild-type retinoschisin plays a role in both retinal cell adhesion [9,13,14] and synaptic integrity between photoreceptors

and bipolar cells [13,15]. Recent elegant studies by several groups have provided evidence for three primary mechanisms that may be responsible for the loss of function of the retinoschisin protein, and therefore pathogenesis of XLRS [9]. The first of these involves misfolding of the discoidin domain, which negatively influences the putative adhesive properties of the protein [9]. The second mechanism is that the pathogenesis is caused by defective disulfide-linked subunit assembly of RS1 into dimers and octamers, which is also presumed to be critical for the proper function of the protein [8]. Lastly, an inability of RS1 to insert into endoplasmic reticulum membrane as part of the protein secretion process is a plausible mechanism for the retinal pathogenesis of XLRS [8,16]. Numerous studies [9,16,17] have demonstrated that in both COS-7 and Weri-Rb1 cultures, cells expressing constructs with mutations known to be pathogenic were retained intracellularly, rather than being secreted like the wild-type protein [16]. Thus these studies provide further mechanistic evidence for why the disease severity of XLRS is not mutation-dependent.

Within the last 20 years, the mouse has been established as an excellent model system for hereditary human diseases. The mouse has also a gene homologous to the human *RS1*, which is referred to as *Rs1h* (retinoschisis-1 homolog) [18]. Although two knockout (KO) models have been reported for the *Rs1h* gene [19,20], no spontaneous or ENU-induced mutant has been described up to now.

Within the TMGC, we have generated and characterized an ENU-induced mutant mouse pedigree with a retinal phenotype. Both retinal structure and function are affected in the *44TNJ* mouse. Mutation analysis demonstrates a mutation in intron 2 of *Rs1h*, which leads to two novel splice variants. The *44TNJ* pedigree has no other systemic or behavioral abnormalities, which is not surprising given that Rs1 is a retina-specific protein [19,20] (a complete listing of all phenotyping examinations performed on *44TNJ* mice by the various domains of the TMGC is available at the TMGC website). This is the first description of an ENU-induced murine model of XLRS and will serve as a valuable resource to study the function of the *Rs1h* gene and its protein product.

METHODS

Animal husbandry: Use of mice in this study was in compliance with the Guiding Principles in the Care and Use of Animals (DHEW Publication NIH 80-23), and was approved by the Animal Care and Use review board of the University of Tennessee Health Science Center and Oak Ridge National Laboratories (Oak Ridge, TN). The mice at the GSF-National Research Center for Environment and Health at Neuherberg, Germany were kept according to the Declaration of Helsinki and the regulations of the German Law on Animal Protection. Mice were maintained at 20 to 24 °C on a 14/10 h light/dark cycle at the University of Tennessee Health Science Center and on a 12/12 h light/dark cycle at GSF-National Research Center for Environment and Health. Animals were fed Agway Prolab 3000 or Altromin mouse chow and given tap water in glass bottles. While the majority of the mice examined in these studies were 10 weeks old, additional *44TNJ* mice at various ages ranging from two weeks to 18 months were utilized in evaluating the ocular phenotype of this ENU-induced mutant mouse.

Generation of the ENU-induced mutant 44TNJ *mice:* Using an ENU mutagenesis strategy, the *44TNJ* pedigree was derived from one C57BL/6JRn founder male mouse that was mated with a C3BLiA-*Eh*/+ female. Subsequently, a breeding scheme was followed such that genetically homozygous test class mice were generated by the third generation (G_3) of breeding. The fourth and subsequent generations should all carry the abnormal recessive mutation generated by the ENU-mutagenesis event. More details about this breeding protocol can be found at the neuromutagenesis domain of the TMGC website. Additional details regarding our mutagenesis program are described elsewhere [21-23]. *44TNJ* mice are available to the scientific community through the TMGC website or through the Neuromice Consortium, a collaborative consortium that maintains and distributes the mutant mice generated through the TMGC, Northwestern University, and The Jackson Laboratories ENU-mutagenesis projects.

The *17TNK* pedigree was used as a control throughout this manuscript and was found to be within normal limits in all tests by all domains of the TMGC. This pedigree was identical to the *44TNJ* pedigree in all respects regarding background strain, mutagenesis with ENU, and husbandry.

Slit lamp and fundus examinations: Mice from the *44TNJ* pedigree were clinically examined when they were approximately 10 weeks old. Mice were lightly anesthetized with an intraperitoneal injection of Avertin (1.25% 2,2,2-tribromoethanol and 0.8% tert-pentyl alcohol in water, 0.3 ml). The anterior segment was examined with a slit lamp biomicroscope (Carl Zeiss, Germany). 1% Cyclomydril ophthalmic drops (Alcon Pharmaceuticals, Fort Worth, TX) were used to dilate the pupil. The fundi were examined by indirect ophthalmoscopy and photographs were taken with a Kowa Genesis small animal fundus camera (Torrance, CA) with the aid of a 90 D condensing lens (Volk, Mentor, OH) as described previously [22,23]. 160T slide film (Kodak, Rochester, NY) was used for photodocumentation.

Table 1. Primers for PCR amplification of the candidate gene *Rs1h*

Designation	Sequence (5'-3')	Tm (°C)	Fragment size (bp)
Rs1h-3L	TGGCTATGAAGCCACATTGGG	63 °C	679
Rs1h-4R	CCCAAAGCTCTCCCTGCAAGTG		
Rs1h-L	CACTTAGATCTTGCTGTGACCAAGGAC	65 °C	190
Rs1h-R	CAGACCACAGAGCATTGGCTCC		
Rs1h-5UTR-L	CTTAATCTCTATGGCATTGTTTTCATTTTGC	66 °C	326
Rs1h-Intron1-R	CTCATGCCCACACCCAACACC		
Rs1h1iL	TGCCCTGCTCCTATGCCAGC	46 °C	244
Rs1h2iR	TACCCCTCAGCACTCTTCCCC		

Listed in the table are the sequences for the primers used to amplify the mouse Rs1h gene from genomic or cDNA, the DNA melting temperature (Tm), and the predicted fragment size of the PCR product. cDNA was used as a template with primers pairs Rs1h-3L/Rs1h-4R and Rs1h-L/Rs1h-R. Genomic DNA was used as a template with primer pairs Rs1h-5UTR-L/Rs1h-Intron1-R and Rs1h1iL/Rs1h2iR.

Fundus images from 112 10 week old *44TNJ* mice were evaluated for ocular abnormalities. A grading system was used in which a normal fundus was graded as 1, a fundus that presented with small focal intraretinal microflecks throughout the posterior pole was graded as 2, and a fundus that presented with larger streak-like flecks in addition to intraretinal microflecks was graded as 3.

Light microscopy: Mice were sacrificed by cervical dislocation and eyes were removed immediately. All histological and immunohistochemical assessments were performed on the same eyes, rather than separate eyes being utilized for each type of analysis. Moreover, all images that are presented for a particular age of mouse are from the same eye and retinal area. The left eyes of eight 10 week old mice from the *44TNJ* pedigree with fundus abnormalities were processed for paraffin embedding and histological/immunohistochemical evaluation. Both eyes from an 18 month old male mouse from the *44TNJ* pedigree were similarly prepared. The left eyes from four 10 week old mice from the *17TNK* pedigree were used as normal controls. Eyes were fixed in 4% paraformaldehyde in 0.06 M phosphate buffer for 24 h, then they were transferred to 0.06 M phosphate buffer. Embedding and sectioning were performed using standard protocols. The orientation of the eyes during the embedding process was controlled so that the anterior-posterior axis of the eye was parallel to the cutting surface of the block. Tissue sections taken from the posterior pole of each eye were stained with hematoxylin and eosin (H&E) using standard protocols. Sections were viewed on an Eclipse E800 microscope (Nikon Inc., Tokyo, Japan) equipped with a color camera (Photometrics, Tuscon AZ), and images of the retina within 1 to 2 mm of the optic nerve head were collected with MetaMorph software (Universal Imaging Corporation, West Chester, PA). Adobe Photoshop 7.0 (San Jose, CA) was used to prepare the final figures.

Immunohistochemistry: Paraffin sections were utilized for immunohistochemical analysis. After removal of the wax, sections were incubated in 1% H_2O_2 for 5 min and rinsed in phosphate buffered saline with 1% Tween-20 (PBS-T). Sections were incubated in primary antibody in PBS-T containing 5% goat serum overnight. The following primary antibodies were used in these studies: anti-GFAP (Immunon, 1:50 dilution) and anti-calbindin D-28K (1:250 dilution; Chemicon, Temecula, CA). These antibodies were selected due to the histological appearance of the retinas from *44TNJ* mice; alterations in GFAP staining would be indicative of an overall nonspecific retinal pathology, while alterations in calbindin labeling would illustrate aberrations of the outer plexiform layer. Control sections were incubated in PBS-T containing 5% goat serum in the absence of primary antibody. Sections were then rinsed in PBS-T and incubated in anti-rabbit secondary antibody in PBS-T containing 5% goat serum for 1 h. The ABC kit (Vectorstain; Vector Laboratories, Inc., Burlingame, CA) was used to visualize the immunolabeling using the protocol suggested by the manufacturer. Sections were viewed on an Eclipse E800 microscope as described above.

Ultrastructure: The right eyes from three mice from the *44TNJ* pedigree from three different ages were processed for more detailed evaluation of subcellular ultrastructure. The following ages of *44TNJ* mice were utilized: 2 weeks, 14 weeks, and 38 weeks. These eyes were fixed in a mixed aldehyde consisting of 2% formalaldehyde and 2% glutaraldehyde in 0.06 M phosphate buffer for 24 h. The anterior segment of each eye was removed prior to further processing. Eyecups were dehydrated through a series of increasing ethanol concentrations and were embedding in Epon812 (EMS, Fort Washington, PA). Similar to eyes processed for paraffin sectioning, the orientation of the eyes was controlled so that the anterior-posterior axis of the eye was parallel to the cutting surface of the block. Thick sections were cut at 1 μm thickness through the posterior pole of the eye. Representative tissue sections were stained with Toluidine blue O. Sections were viewed on an Eclipse E800 microscope (Nikon Inc., Tokyo, Japan) as described above. Thin sections were cut and viewed on a JEOL JEM1200EX II electron microscope.

Electroretinography: Mice were dark-adapted overnight and anesthetized with a mixture of ketamine/xylazine (80 mg/kg and 16 mg/kg, respectively). Their pupils were dilated with 1% tropicamide, 1.5% cyclopentolate. A small wire loop electrode contacting the cornea through a layer of methylcellulose recorded the response from the retina, while a needle electrode placed in the cheek and tail served as reference and ground, respectively. Each mouse was placed in front of a Ganzfeld bowl (LKC Technologies, Inc., Gaithersburg, MD) that presented a series of flashes with increasing intensity (-3.0 to 2.1 log cd sec/m^2). To isolate cone responses, an intensity series (-0.82 to 1.8 log cd sec/m^2) was presented with a 30 cd/m^2 adapting field. Amplitude and implicit time measurements were recorded and compared between one eye of each 44TNJ mutant (n=4) and 17TNK control mouse (n=5). Statistical analysis of the relationship between amplitude and intensity was performed using repeated measure ANOVA with an α level of 0.05. To select for mutant mice, ERGs were performed at the GSF-National Research Center for Environment and Health, as described previously [24].

Gene mapping and mutation analysis: Gene mapping and mutation analysis were performed at both UTHSC and at the GSF-National Research Center for Environment and Health in Neuherberg. At UTHSC, F1 mice were generated by crossing *44TNJ* affected female mice with C3BLiA male mice. F2 mice were produced by brother-sister matings. Mutant mice were identified by the fundus features and histological assessment. To narrow the genetic interval harboring the mutation, DNA was obtained from the tails of a set of 55 F2 mice. Microsatellite primer pairs were purchased from Invitrogen Life Technologies (Carlsbad, CA). PCR reactions were carried out in 96 well microtiter plates. A high-stringency touchdown protocol was used in which the annealing temperature was lowered progressively from 60 °C to 50 °C in 2 °C steps over the first 6 cycles [25]. After 30 cycles, products from the PCR reactions were run on 2.5% Metaphor agarose gels (FMC Bioproducts, Rockland ME), stained with ethidium bromide, and photographed. After an initial analysis using MIT microsatellite loci distributed across all autosomes and the X chromosome, the following microsatellite primer pairs were

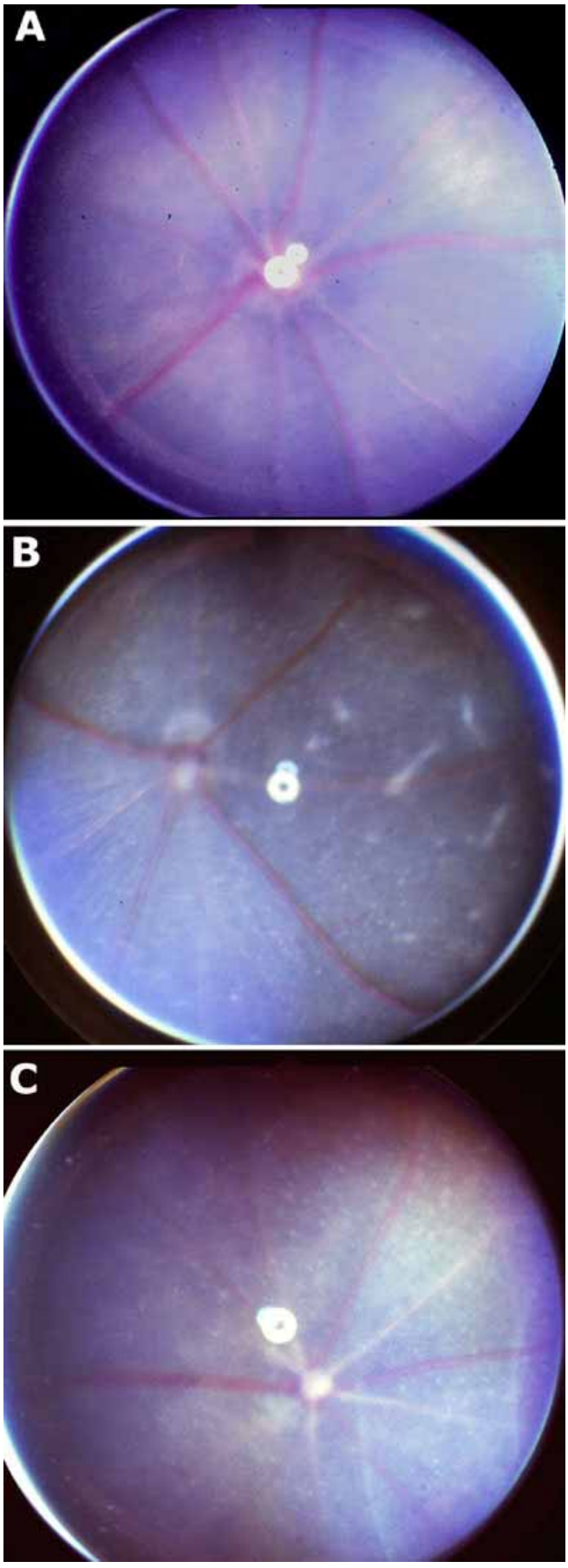

used to narrow the interval containing the mutation: *DXMit89*, *DXMit166*, *DXMit144*, *DXMit1*, *DXMit61*, *DXMit172*, *DXMit173*, *DXMit38*, and *DXMit186*. Similar to our previous study [26], genome-wide significance levels for assessing the confidence of the linkage statistics were estimated by comparing the peak likelihood ratio statistic (LRS) using the MapManager QTX program (version b17). The LRS can be converted to the conventional base-10 LOD score by dividing it by 4.61 (twice the natural logarithm of 10). The LRS is statistically convenient because its distribution is asymptotically a χ^2 distribution [27].

At the GSF-National Research Center for Environment and Health in Neuherberg, mice without the C3BLiA background were used to establish an independent line. Male carriers were mated to wild-type DBA/2 mice and F1 progeny were backcrossed to the *44TNJ* mutant mice. Mutant mice were identified using ERG analysis. Genomic DNA was prepared from tail snips of 92 mice from the F2 progeny according to standard procedures. A linkage analysis was performed using the two microsatellite markers *DXMit227* and *DXMit117*, located at 28.4 and 50.8 cM, respectively, using PCR primers produced at the GSF-National Research Center for Environment and Health. The cDNA was synthesized from mRNA isolated from entire eyes (stored at -80 °C) of adult mice according to standard procedures. For the PCR amplification of the mouse *Rs1h* gene, genomic or cDNA was used as a tem-

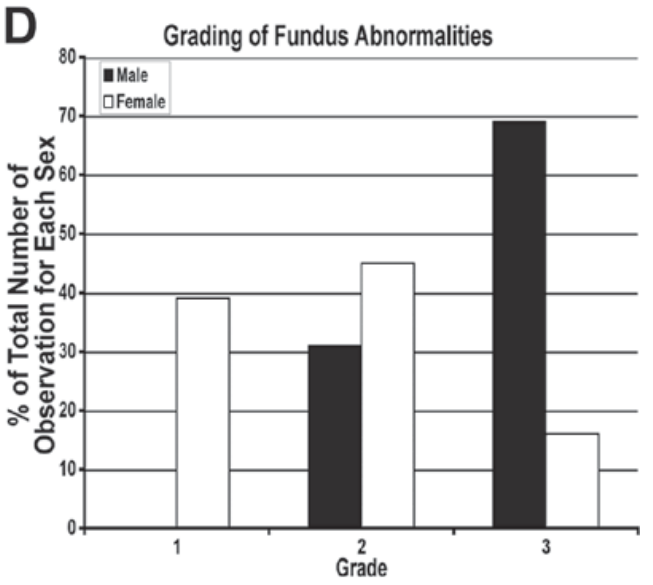

Figure 1. Fundus images and grading of fundus abnormalities. Representative fundus images from a male *17TNK* control mouse (**A**), a male *44TNJ* mouse with both intraretinal flecks and streaks throughout the posterior pole (**B**), and a female *44TNJ* mouse with only intraretinal flecks (**C**) are shown. **D**: A histogram of fundus grade using our scale (grade 1: normal fundus; grade 2: fundus that presents with small focal intraretinal microflecks; grade 3: fundus that presents with larger streak-like flecks in addition to intraretinal microflecks) shows that 100% of the male G_4 *44TNJ* mice have fundus abnormalities, while only 61% of the female mice from G_4 present with fundus flecks or streaks.

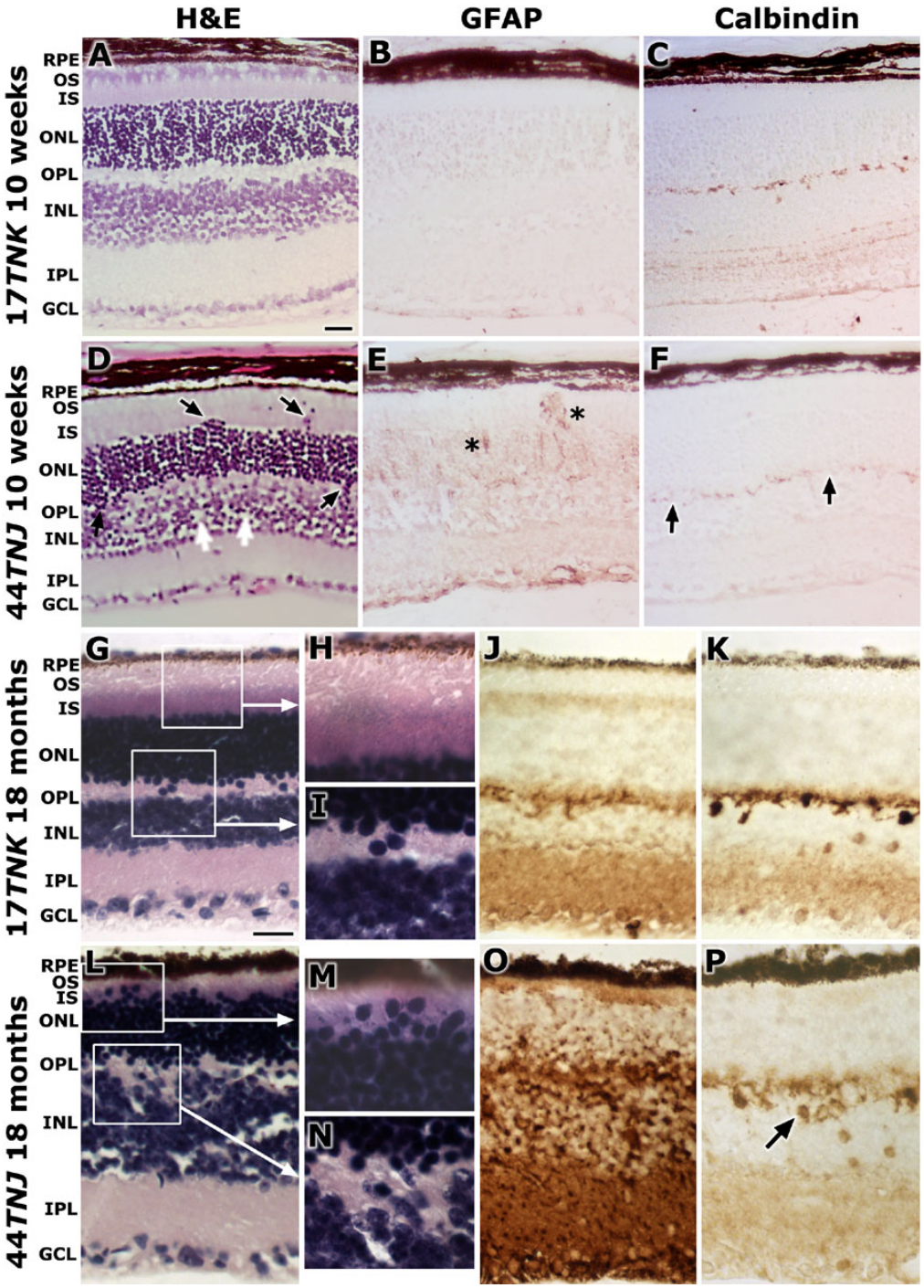

Figure 2. Histological and immunohistochemical analyses of retinas from control and *44TNJ* mice at 10 weeks and 18 months. Representative images of retinal structure (**A**) and immunohistochemical localization of GFAP (**B**) and calbindin (**C**) from 10 week old *17TNK* control mice are shown; while retinal sections from 10 week old *44TNJ* mutant mice are illustrated in **D**, **E**, and **F**, respectively. Note the displacement of photoreceptor nuclei (black arrows) and the focal splitting of the INL (white arrows) in retinas from *44TNJ* mice (**D**). GFAP immunolabeling was elevated in the retinas of mutant mice (asterisks in **E**). In contrast, calbindin immunolabeling was decreased in those same mice (black arrows in **F**). Similar representative images from 18 month old mice are illustrated in **G**-**P**. With aging, there is no change in retinal structure in the *17TNK* control mice (**G**-**I**). However, the intensity of the GFAP (**J**) and calbindin (**K**) immunolabeling increased slightly. In the retinas from 18 month old *44TNJ* mice, there was a shortening of photoreceptor inner segments (IS) and outer segments (OS; **L**,**M**) along with further displacement of nuclei into the areas of IS, OS and the outer plexiform layer (OPL; **L**,**N**). Moreover, the inner nuclear layer (INL) appeared to split, thus allowing the OPL to fill the gaps (**L**,**N**). GFAP levels were greatly increased (**O**) over the age-matched controls. Calbindin labeling was reduced in intensity and many calbindin-positive horizontal cells were localized deeper into the INL (black arrow in **P**). The retinal pigment epithelium (RPE), outer nuclear layer (ONL), inner plexiform layer (IPL), and ganglion cell layer (GCL) are also identified. Scale bars represent 10 μm.

plate, which was then amplified using the corresponding forward and reverse primers (Table 1). PCR products were sequenced commercially (SequiServe, Vaterstetten, Germany) after cloning into the pCRII Vector (Invitrogen, Karlsruhe, Germany) or after elution from the agarose gel using kits from Macherey & Nagel (Düren, Germany) and subsequent precipitation by ethanol and glycogen. To confirm the mutation, the PCR product (326 bp) from genomic DNA was digested by the restriction enzyme *Nla*III

RESULTS

Fundus phenotype: The fundi of control mice from the *17TNK* pedigree were evenly pigmented (n=8; Figure 1A). In the fundi of male *44TNJ* mice, there were many intraretinal microflecks throughout the posterior pole along with less-frequent, larger, more streak-like manifestations (Figure 1B). Most female *44TNJ* mice presented with intraretinal microflecks, which were typically small and homogeneous within 3 disk diameters around the optic nerve head (Figure 1C). Application of our grading scale to the fundus photographs indicated that all

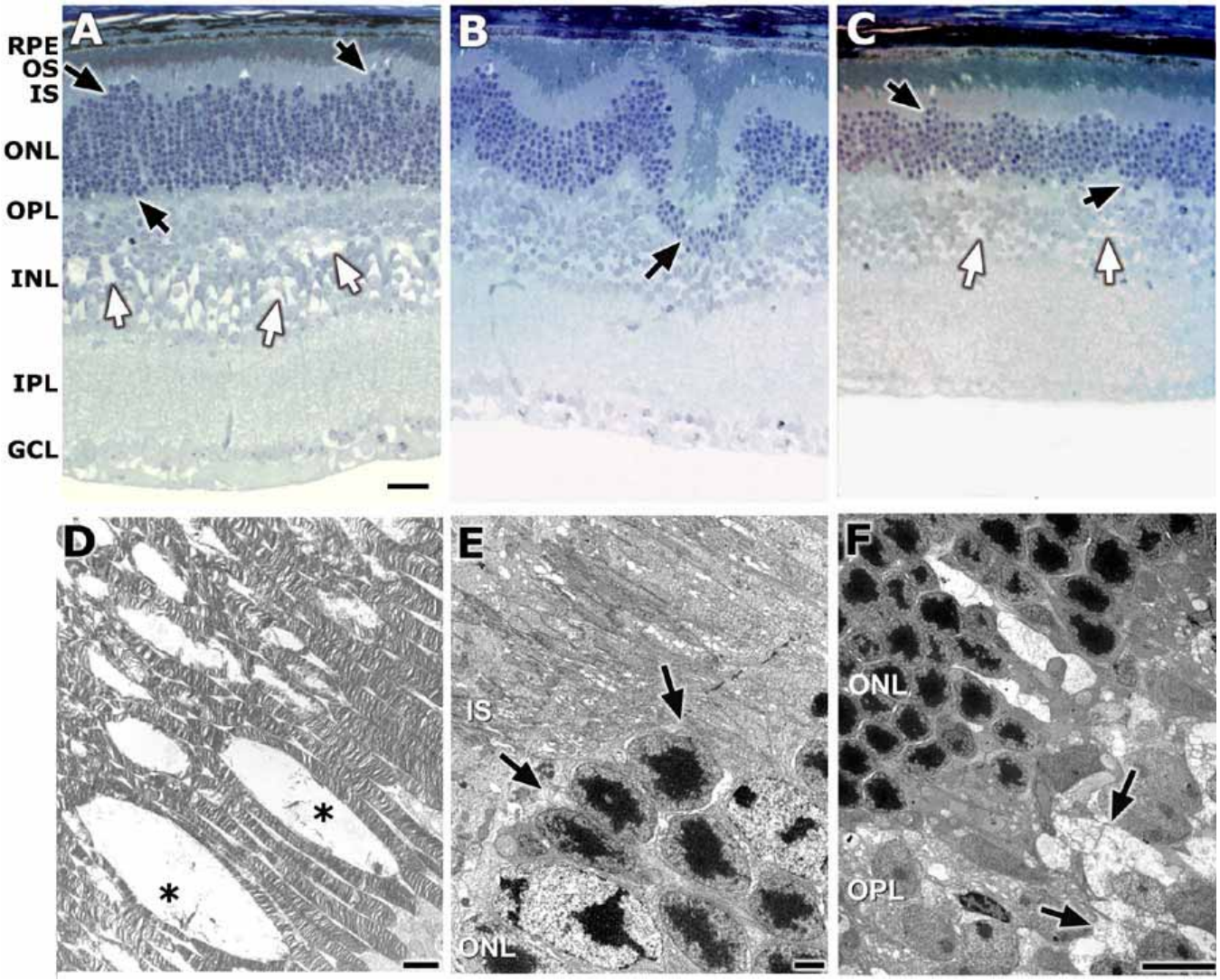

Figure 3. Detailed structural analysis. Light-level histology and electron microscopic images of the retinas of male *44TNJ* mutant mice at various ages are presented in this figure. Representative images of retinal structure from 2 week (**A**), 14 week (**B**), and 38 week (**C**) *44TNJ* mutant mice are shown. Displacement of photoreceptor nuclei (black arrows) and schisis of the inner nuclear layer (INL; white arrows) are present as early as 2 weeks (**A**). The same morphological features are present with no progression until 38 weeks (**C**). Less frequently, large clusters of displaced nuclei appear to have migrated into the INL (arrow in **B**). **D**-**F**: Representative electron micrographs taken from the 14 week old *44TNJ* mouse are shown. **D**: Gaps are present between outer segments (OS) with occasional debris (asterisks). **E**: In areas where the photoreceptor nuclei are displaced into the inner segments (IS), the adherens junctions that comprise the outer limiting membrane are absent (arrows). **F**: The outer plexiform layer (OPL) structure is disrupted and filled with debris (arrows). The retinal pigment epithelium (RPE), outer nuclear layer (ONL), inner plexiform layer (IPL), and ganglion cell layer (GCL) are also identified. Scale bars represent 20 μm in **A**-**C** and 2 μm in **D**-**F**.

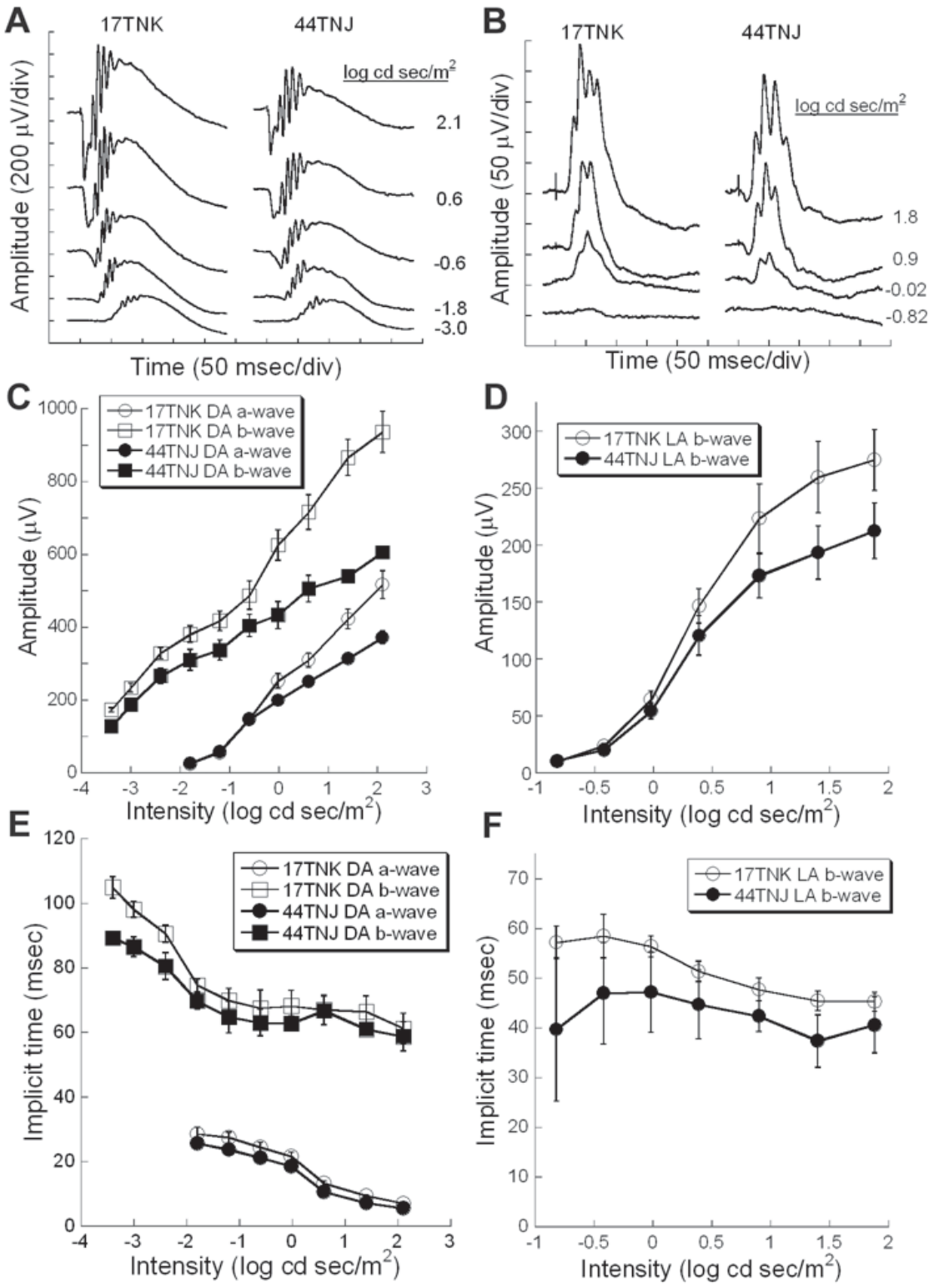

Figure 4. Electroretinography recordings from *44TNJ* mice compared to *17TNK* controls. Dark-adapted (**A**) and light-adapted (**B**) ERG waveforms from *17TNK* and *44TNJ* in response to increasing flash intensities are shown. Each waveform is the average of 5-10 responses recorded from a representative mouse. **C**: ERG a- and b-wave amplitude values for each stimulus tested under dark-adapted conditions are shown. The *44TNJ* mice have significantly reduced responses at brighter flash intensities compared to *17TNK* mice. **D**: Light-adapted ERG amplitudes across the flash intensities tested. Differences between mutant and control responses at the same intensities are not statistically significant. Implicit time (**E**) for the dark-adapted responses showed no differences between mutant and control mice across flash intensities. The implicit time of the light-adapted responses (**F**) in the *44TNJ* mice were significantly faster than *17TNK* controls. All error bars represent standard error of the mean.

male mice presented with an abnormal fundus phenotype, such that all male mice had a grade of either 2 or 3 (Figure 1D). Of the 45 male mice that were examined, 31% presented with only intraretinal flecks (grade 2), while the remaining 69% presented with both flecks and streaks (grade 3). Of the 67 female mice that were examined, 39% had a normal fundus appearance (grade 1), as compared to 45% that had only flecks (grade 2) and 16% that had both flecks and streaks (grade 3).

Retinal histology and immunohistochemical findings in the retinas of 10 week old male mice: The histological examination of retinas from 10 week old *17TNK* male mice (n=4) were normal in all aspects. H&E stained tissue sections showed normal lamination, integrity of the RPE, and presence of photoreceptor outer segments (Figure 2A). In these same retinas, the immunoreaction product for GFAP was negligible in all layers of the *17TNK* retinas (Figure 2B). Calbindin immunostaining revealed dense and continuous labeling in the outer plexiform layer with both the cell bodies and lateral processes of horizontal cells being labeled (Figure 2C).

In contrast, the histological examination of all eyes from eight *44TNJ* male mice (Figure 2D) revealed a disruption of the lamination of the retina including migration of clusters of photoreceptor nuclei into the area of the inner and occasionally outer segments of the photoreceptors. These clusters of displaced nuclei very likely correspond to the microflecks that were evident on the fundus examination. The outer plexiform layer was periodically disrupted with cell bodies from the inner and outer nuclear layers abutting each other. Focal areas of inner nuclear layer splitting were also evident. At 10 weeks of age, the level of GFAP immunostaining was slightly elevated compared to control and radial patterns of Müller cell labeling were apparent (compare Figure 2E,B). Evaluation of calbindin-immunostained sections revealed a discontinuous and weak labeling pattern in the outer plexiform layer (Figure 2F).

Retinal histology and immunohistochemical findings in the retinas of 18 month old mice: Histological and immunohistochemical analyses of both eyes of one 18 month old *17TNK* control mouse indicated that both the structure (Figure 2G-I), and the immunolabeling patterns of anti-GFAP (Figure 2J) and anti-calbindin (Figure 2K) were similar to 10 week old mice control mice. There was a slight increase in GFAP immunolabeling in the inner retina, which is a common phenomenon in the retinas of aged mice [22]. In both eyes of the aged *44TNJ* mouse, however, there were some marked changes. There were many photoreceptor nuclei that migrated into the area of inner and outer segments, and the combined length of the inner/outer segments was very short compared to those of the age-matched *17TNK* control mouse (Figure 2L,M, compare to Figure 2G,H). Moreover, in some areas, the outer plexiform layer had expanded deeper into the inner nuclear layer (Figure 2L,N). The areas of schisis within the inner nuclear layer were still prominent in the retinas from the aged mouse. There was a marked increase in the immunolabeling of Müller cells by the GFAP antibody (Figure 2O) compared to both the age-matched control (Figure 2J) and 10 week old *44TNJ* mice (Figure 2B). The immunolabeling of horizontal cells with anti-calbindin antibodies demonstrated that the level of immunolabeling continued to be lower than its age-matched control (compare Figure 2P,K). In addition, it appeared that by 18 months, there was a migration of horizontal cells and their processes deeper into the inner nuclear layer, thus corresponding very well with the apparent expansion of the outer plexiform layer as shown histologically in Figure 2N.

Retinal ultrastructure at various ages: An evaluation of retinal structure was undertaken for the dual purpose of determining whether the aberrations in retinal lamination were due to a developmental defect and also if the retinal phenotype was progressive in nature. Our results indicated that as early as two weeks, the retina had all of the aberrant structural features that we documented at ten weeks of age (Figure 3A). Photoreceptor nuclei were present in the area of the inner segments, beyond the outer limiting membrane, and in the area of the outer plexiform layer. Moreover, there were areas of schisis present in the inner nuclear layer. At 14 weeks (Figure 3B), these same morphological characteristics were present in addition to rosette-like structures in the outer nuclear layer projecting deep into the inner nuclear layer. The small clusters of photoreceptor nuclei may correspond to the microflecks on the fundus examination, while the rosettes likely correspond to the streak-like patterns that are prominent on the fundus examination. At 38 weeks (Figure 3C), the morphological characteristics of the retina did not differ from that of retinas from younger mice, suggesting that up to 38 weeks, there is no marked histologic progression of the phenotype of *44TNJ* mice.

Ultrastructural analysis of the retina of 14 week old male *44TNJ* mice indicated that many aspects of retinal structure were compromised in this mutant mouse. The photoreceptor outer segments (Figure 3D) had focal gaps between adjacent outer segments with some membranous remnants filling those spaces. In areas where photoreceptor nuclei had migrated into the area of photoreceptor inner segments, there was a complete absence of the adherens junctions that are typically formed between Müller cells and the photoreceptors with which they are closely associated (Figure 3E). Moreover, the outer plexiform layer was disorganized and contained extracellular gaps filled with debris (Figure 3F).

ERG findings: Figure 4A shows the ERG intensity response series recorded under dark-adapted conditions from representative *17TNK* control (left side) and *44TNJ* mutant mice (right side) at four months of age. At the lowest flash intensity, the ERG response from both strains of mice contained the positive b-wave generated by the activity of the bipolar cells [28-31]. As the flash intensity increased, the negative a-wave generated by the photoreceptors [32,33] became visible and then both waves became larger and faster. Note the wavelets or oscillatory potentials on the leading edge of the b-wave in both strains. The only difference in the response between the two strains was a reduced amplitude of a- and b-waves in the *44TNJ* mice. The difference in dark-adapted response amplitude can be seen more clearly in Figure 4C, which shows the dark-adapted a- and b-wave amplitudes across each

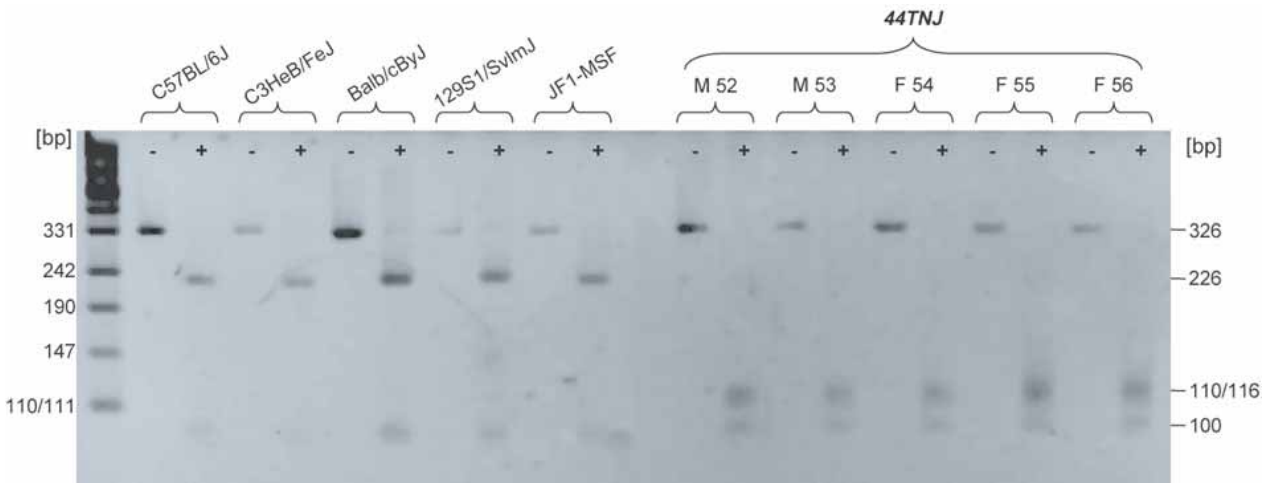

Figure 6. *Nla*III digestion of genomic DNA. *Nla*III digestion of genomic DNA illustrates a new restriction site that was introduced by the mutation in *Rs1h*. Wild-type mice of different strains (C57BL/6J, C3HeB/FeJ, BALB/cByJ, 129S1/SvlmJ, and JF1-MSF) served as controls. Six different *44TNJ* mice were test for the transition (T->C) of the second base pair of intron 2, which creates an additional *Nla*III restriction site.

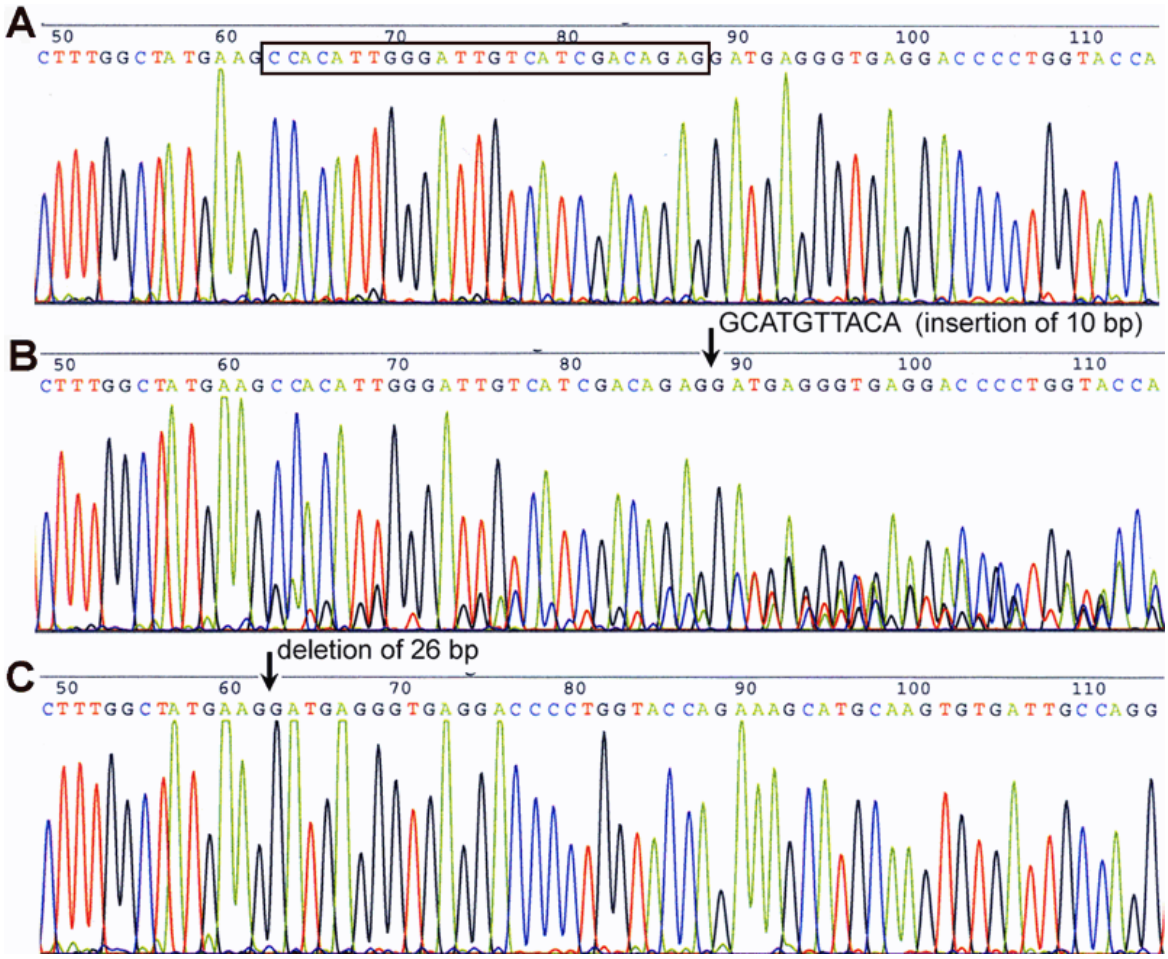

Figure 5. Sequencing analysis of *Rs1h*. The amplified cDNA of a wild-type mouse and two amplification products of different sizes from a *44TNJ* mutant mouse were sequenced. **A**: Wild-type control. **B**: Sequence of transcript 1 from the *44TNJ* mutant of normal size, showing a double sequence caused by a splice variant with a 10 bp deletion. The beginning of the double sequence is marked with an arrow. A third sequence with smaller peaks starting at position 63 corresponds to transcript 2. **C**: Sequence of transcript 2 from the *44TNJ* mutant with a 26 bp deletion.

flash intensity presented. While the *44TNJ* mice showed near normal responses with dim flashes, there were significant reductions in amplitude at higher flash intensities (a-wave: $F_{6,36}$ =9.48, p<0.0001; b-wave $F_{9,54}$=13.46, p<0.0001). Figure 4E demonstrates no difference in implicit time between responses from the *44TNJ* mutant and *17TNK* control mice.

Figure 4B shows representative the light-adapted responses, which isolated the cone response from a single *17TNK* control and *44TNJ* mutant mouse. The b-wave became clearly visible in the second step of the intensity series (-0.02 log cd sec/m^2) and then grew in amplitude with increasing flash intensity. While the *44TNJ* mice showed a slight reduction in light-adapted b-wave amplitude compared to *17TNK* animals, the difference did not reach significance (Figure 4D; $F_{6,42}$=2.05, p=0.08). However, the implicit time for the light-adapted responses did show significantly faster responses for the *44TNJ* mice, although this may be due to the variability in oscillatory potentials. (Figure 4F; $F_{6,42}$=5.394, p<0.001).

Genetic analysis: The DNA from 55 male affected F_2 mice were genotyped at UTHSC. The results indicated that the *44TNJ* mutation mapped to the X Chromosome. The interval map was determined using two phenotypes, namely fundus appearance and retinal structure derived from H&E stained paraffin sections. This locus includes the markers from *DXMit61* (30.9 cM) to *DXMit186* (69.0 cM); the corresponding LRS scores were 11.4 and 24.0, respectively. A maximum LRS score of 24 was obtained for linkage to *DXMit186* (χ^2 for males=40).

For fine mapping of the X-chromosome, 92 mice from the F_2 progeny were genotyped at the GSF using the two markers *DXMit227* and *DXMit117*, located at 28.4 and 50.8 cM, respectively. Highly significant linkage was found to marker *DXMit117* (χ^2 for males=23.5). Calculating the recombination frequency, it was estimated that the mutation should be located 21±6 cM distal of this marker, since the proximal marker *DXMit227* at the position 28.4 cM did not show a significant linkage (χ^2 for males=1.4).

Because of the critical position of about 70 cM, the retinoschisis-1 homolog gene *Rs1h* was tested as candidate of the *44TNJ* mutation. Amplification of the *Rs1h* cDNA from *44TNJ* mutants revealed two PCR products instead of a single one, as was found in the wild-type mouse (Figure 5A). Sequencing of the larger PCR product of *44TNJ* mice revealed a "mixed" sequence (Figure 5B). One part was the wild-type sequence, the other part showed a frameshift caused by a 10 bp insertion. This 10 bp insertion was identical to the first base of intron 2 with the exception of a T to C change at the second base. The sequence analysis of the smaller fragment of the *44TNJ-Rs1h* cDNA revealed a 26 bp deletion also at the transition from exon 2 to intron 2 (Figure 5C).

To confirm this mutation at the genomic level, we amplified a 326 bp fragment of genomic DNA covering this critical position. The T to C exchange creates a new restriction site for *Nla*III, which was not present in the wild-type (Figure 6). We confirmed the presence of this novel restriction site in five male hemizygous mice with the mutation, however, we did not find this restriction site in any of the five different wild-type controls of C57BL/6J, C3H, BALB/c, 129, and JF1 mice (Figure 6). Therefore, the *44TNJ* mutation should be referred to as a new allele of the *Rs1h* gene, *Rs1h*^{44TNJ}.

Computer assisted translation of the novel *Rs1h* splice products in the *44TNJ* mutants revealed the formation of premature stop codons because of the frameshift caused by both the 10 bp insertion and the 26 bp deletion (Figure 7). In case of the 26 bp deletion (corresponding to the entire exon 2), the new open reading frame reaches a new stop codon immediately at the beginning of exon 3, thus resulting in a truncated protein that consists only of the first 17 amino acids plus an additional new one. In case of the 10 bp insertion after exon 2, the first 26 amino acids were present, followed by four new amino acids and a premature stop codon at the beginning of exon 3. In both cases, after only a few bases, other open reading frames were present, which might be used also by the translation machinery. Further experiments are needed to clarify whether the short mutated N-terminal Rs1h peptides are present in the retina or whether the corresponding mutant mRNAs are degraded because of nonsense-mediated decay. Similarly, future experiments will address the question of whether the pro-

```
                      Exon 1      intron 1          Exon 2             | intron 2            Exon 3
wt genomic DNA*:     TTTGGCTATGAAGgtatgt...gctcagCCACATTGGGATTGTCATCGACAGAGgtatgttacagtaa...cttgcagGATGAGGGTGAG
44TNJ genomic DNA:   TTTGGCTATGAAGgtatgt...gctcagCCACATTGGGATTGTCATCGACAGAGgcatgttacagtaa...cttgcagGATGAGGGTGAG
                                                                          -—-
wt transcript:       TTTGGCTATGAAG            CCACATTGGGATTGTCATCGACAGAG                        GATGAGGGTGAG
wt protein:           F  G  Y  E              A  T  L  G  L  S  S  T  E                          D  E  G  E

44TNJ transcript 1:  TTTGGCTATGAAG            CCACATTGGGATTGTCATCGACAGAGgcatgttaca              GATGAGGGTGAG
44TNJ protein 1:      F  G  Y  E              A  T  L  G  L  S  S  T  E  A  C  Y                R Stop

44TNJ transcript 2:  TTTGGCTATGAAG                                                              GATGAGGGTGAG
44TNJ protein 2:      F  G  Y  E                                                                G Stop
```

Figure 7. *Rs1h* mutation in *44TNJ* mice. The intronic mutation in *Rs1h* results in alternative splice products and short peptide transcripts. The designation of the intron/exon boundaries follows the data given by Gehrig et al. [18], which is in agreement with our sequencing data (Figure 5). These sequences are different from the predicted data given by the ENSEMBL version (checked on May 28, 2005). Exon sequences are given in uppercase letters, intron sequences in lower case letters. The T to C exchange in intron 2 is indicated by a green/red color flip and a vertical red bar; the bases of the new *Nla*III restriction site in the mutant sequence are in red. The stop codons in the new *44TNJ* transcripts are marked with hyphens. The premature stop in the protein sequence is highlighted in red.

teins encoded by the new open reading frames are present in the retina.

DISCUSSION

Herein we characterize and present the ocular phenotype of an ENU-induced mutant mouse with a novel mutation located in an intronic sequence of *Rs1h*. While there have been previous reports of *Rs1h* KO mice [19,20], this is the first presentation of a murine model with a mutation in *Rs1h*. The previous *Rs1h* KO mice presented with the morphologic phenotypes of retinal layer disruption indicated by displaced photoreceptor nuclei and dissection or schisis of the inner nuclear layer of the retina. Moreover, these mice had a disruption of synaptic structure in the outer plexiform layer where photoreceptors synapse on second order neurons, such as bipolar cells. As expected, given the morphologic phenotype, the b-wave of the scotopic ERG response was significantly reduced in the *Rs1h* KO mice generated by both groups [19,20]. Zeng et al., however, also demonstrated a reduced a-wave amplitude in their KO mice, which correlated well with the shortened photoreceptor inner and outer segments that they documented [19,20].

The morphological and functional phenotype of *44TNJ* mice is strikingly similar to both *Rs1h* KO mice. The *44TNJ* mice have similar displacement of photoreceptor nuclei both distally and proximally. Moreover, we demonstrate a reduced and discontinuous calbindin labeling pattern that correlates well with the disruption of the outer plexiform layer as seen morphologically. Coupled with this are dissections or splitting of the inner nuclear layer. ERG analyses indicate a reduced contribution of both photoreceptors and second order neuron function in these mutant mice.

Although not presented in the previous descriptions of *Rs1h* KO mice, we demonstrate the presence of intraretinal flecks upon fundus examination in all males, and in 61% of the females. Often the severity of the fundus features was increased by the presence of larger intraretinal streaks. Morphologically, the flecks and streaks likely correlate with the undulating pattern of the outer nuclear layer and the presence of rosettes. The phenotype of the *44TNJ* mice parallels nicely the disease expression variations that have been documented in human families [7]. Female obligate carriers of mutations in *RS1* are typically asymptomatic. Our fundus examinations of 67 female test class mice from the *44TNJ* pedigree indicate that 61% of these mice have fundus features similar to that of the male mice. Although this cohort of mice were not genotyped for mutations in *Rs1h*, these females were likely homozygous for mutations in *Rs1h*, which is due to the breeding scheme that was utilized to generate the G_4 test class mice.

Similar to the human condition [3,4], male hemizygous mutant mice have a retinal phenotype at an early age. The morphological aberrations of the retina are present as early as two weeks of age in the *44TNJ* mice and do not appear to progress up to 38 weeks. At 18 months, however, there appears to be a worsening of the morphological phenotype along with an elevated GFAP response of the Müller glia, which is not due to aging alone [22]. Because the results from the aged mice were obtained from only one mouse of each pedigree, they should not be considered definitive until confirmed in other mice of a similar age. Nonetheless, this result parallels the progression of the disease in humans in which retinal detachments and a further decrease in vision can occur later in life [3].

The mutation in *44TNJ* mouse is a point mutation in *Rs1h* with a T->C substitution in intron 2 at position 2. The net effect of this mutation is introduction of an alternative splice site and the expression of two new splice products in the retinas of the *44TNJ* mutant. The first alternative transcript has a 10 bp insertion between positions 88 and 89, whereas second alternative transcript has a 26 bp deletion at position 62. While neither splice variant encodes for a stop codon at the position of the mutation, both lead to a frameshift and to a premature stop codon slightly downstream of the mutation. Because these stop codons are introduced very early in the sequence of *Rs1h*, it is predicted that only very short peptides will be produced by the alternative splice sites. The predicted truncated protein products of the mutation likely explain the similarity of the phenotype of the *44TNJ* mouse with a point mutation of *Rs1h* and the *Rs1h* KO models previously described [19,20]. The putative abbreviated peptides present in the retinas of *44TNJ* mice likely undergo nonsense-mediated decay of the mutated mRNAs [34], thus equating the *44TNJ* mouse to a hypomorph. Another, although less likely, explanation may be that the gene product of the intronic mutation exerts a “dominant-negative” effect. These hypotheses will need to be experimentally tested before any conclusions can be derived as to the mechanism(s) by which a mutation in intron 2 of *Rs1h* leads to disruption of retinal structure and function.

In humans, approximately 80% of the mutations are missense mutations in the discoidin domain [12,35], which is encoded by exons 4-6. The other 20% of the mutations are present in exons 1-3 and result in altered transcription of the gene with premature truncation or loss of Rs1 expression [36]. While the vast majority of mutations in *XLRS* are located in exons, several recent reports have documented mutations in intronic sequences in the human [37-41]. The *44TNJ* mouse with a point mutation in intron 2 is a novel model for XLRS and would allow for the study of the function of the Rs1 protein that is completely lacking the discoidin domain. Moreover, because the mutation in the *44TNJ* mouse allows for truncated Rs1 protein to be expressed, the disease mechanisms underlying the retinal pathology should be very similar to that of the human disease, thus allowing for many of the recently proposed pathological mechanisms that stem from in vitro studies to be confirmed in vivo and studied in greater depth.

ACKNOWLEDGEMENTS

We thank Mareike Maurer and Kathy Troughton for excellent technical assistance. The work was supported in part by U01-MH61971 (to DG and MMJ), the German National Genome Network (NGFN; 01GR0103 to JG), the Department of Veterans Affairs (to MTP), and unrestricted grants from Research to Prevent Blindness (New York, NY) to the Department of Ophthalmology at the University of Tennessee Health

Science Center (Memphis, TN) and the Department of Ophthalmology, Emory University School of Medicine (Atlanta, GA).

REFERENCES

1. Sauer CG, Gehrig A, Warneke-Wittstock R, Marquardt A, Ewing CC, Gibson A, Lorenz B, Jurklies B, Weber BH. Positional cloning of the gene associated with X-linked juvenile retinoschisis. Nat Genet 1997; 17:164-70.
2. Kellner U, Brummer S, Foerster MH, Wessing A. X-linked congenital retinoschisis. Graefes Arch Clin Exp Ophthalmol 1990; 228:432-7.
3. George ND, Yates JR, Moore AT. X linked retinoschisis. Br J Ophthalmol 1995; 79:697-702.
4. George ND, Yates JR, Moore AT. Clinical features in affected males with X-linked retinoschisis. Arch Ophthalmol 1996; 114:274-80.
5. Sieving PA. Juvenile retinoschisis. In: Traboulsi E, editor. Genetic diseases of the eye. New York: Oxford University Press; 1998. pp. 347-55.
6. Kaplan J, Pelet A, Hentati H, Jeanpierre M, Briard ML, Journel H, Munnich A, Dufier JL. Contribution to carrier detection and genetic counselling in X linked retinoschisis. J Med Genet 1991; 28:383-8.
7. Eksandh LC, Ponjavic V, Ayyagari R, Bingham EL, Hiriyanna KT, Andreasson S, Ehinger B, Sieving PA. Phenotypic expression of juvenile X-linked retinoschisis in Swedish families with different mutations in the XLRS1 gene. Arch Ophthalmol 2000; 118:1098-104.
8. Wu WW, Wong JP, Kast J, Molday RS. RS1, a discoidin domain-containing retinal cell adhesion protein associated with X-linked retinoschisis, exists as a novel disulfide-linked octamer. J Biol Chem 2005; 280:10721-30.
9. Wu WW, Molday RS. Defective discoidin domain structure, subunit assembly, and endoplasmic reticulum processing of retinoschisin are primary mechanisms responsible for X-linked retinoschisis. J Biol Chem 2003; 278:28139-46.
10. Baumgartner S, Hofmann K, Chiquet-Ehrismann R, Bucher P. The discoidin domain family revisited: new members from prokaryotes and a homology-based fold prediction. Protein Sci 1998; 7:1626-31.
11. Vogel W. Discoidin domain receptors: structural relations and functional implications. FASEB J 1999; 13:S77-82.
12. Functional implications of the spectrum of mutations found in 234 cases with X-linked juvenile retinoschisis. The Retinoschisis Consortium. Hum Mol Genet 1998; 7:1185-92.
13. Molday LL, Hicks D, Sauer CG, Weber BH, Molday RS. Expression of X-linked retinoschisis protein RS1 in photoreceptor and bipolar cells. Invest Ophthalmol Vis Sci 2001; 42:816-25.
14. Reid SN, Yamashita C, Farber DB. Retinoschisin, a photoreceptor-secreted protein, and its interaction with bipolar and muller cells. J Neurosci 2003; 23:6030-40.
15. Takada Y, Fariss RN, Tanikawa A, Zeng Y, Carper D, Bush R, Sieving PA. A retinal neuronal developmental wave of retinoschisin expression begins in ganglion cells during layer formation. Invest Ophthalmol Vis Sci 2004; 45:3302-12.
16. Wang T, Waters CT, Rothman AM, Jakins TJ, Romisch K, Trump D. Intracellular retention of mutant retinoschisin is the pathological mechanism underlying X-linked retinoschisis. Hum Mol Genet 2002; 11:3097-105.
17. Grayson C, Reid SN, Ellis JA, Rutherford A, Sowden JC, Yates JR, Farber DB, Trump D. Retinoschisin, the X-linked retinoschisis protein, is a secreted photoreceptor protein, and is expressed and released by Weri-Rb1 cells. Hum Mol Genet 2000; 9:1873-9.
18. Gehrig AE, Warneke-Wittstock R, Sauer CG, Weber BH. Isolation and characterization of the murine X-linked juvenile retinoschisis (Rs1h) gene. Mamm Genome 1999; 10:303-7.
19. Weber BH, Schrewe H, Molday LL, Gehrig A, White KL, Seeliger MW, Jaissle GB, Friedburg C, Tamm E, Molday RS. Inactivation of the murine X-linked juvenile retinoschisis gene, Rs1h, suggests a role of retinoschisin in retinal cell layer organization and synaptic structure. Proc Natl Acad Sci U S A 2002; 99:6222-7.
20. Zeng Y, Takada Y, Kjellstrom S, Hiriyanna K, Tanikawa A, Wawrousek E, Smaoui N, Caruso R, Bush RA, Sieving PA. RS-1 gene delivery to an adult Rs1h knockout mouse model restores ERG b-Wave with reversal of the electronegative waveform of X-linked retinoschisis. Invest Ophthalmol Vis Sci 2004; 45:3279-85.
21. Goldowitz D, Frankel WN, Takahashi JS, Holtz-Vitaterna M, Bult C, Kibbe WA, Snoddy J, Li Y, Pretel S, Yates J, Swanson DJ. Large-scale mutagenesis of the mouse to understand the genetic bases of nervous system structure and function. Brain Res Mol Brain Res 2004; 132:105-15.
22. Johnson DK, Rinchik EM, Moustaid-Moussa N, Miller DR, Williams RW, Michaud EJ, Jablonski MM, Elberger A, Hamre K, Smeyne R, Chesler E, Goldowitz, D. Phenotype screening for genetically determined age-onset disorders and increased longevity in ENU-mutagenized mice. Age 2005; 27:75-90.
23. Jablonski MM, Wang XF, Lu L, Miller DR, Rinchik EM, Williams RW, Goldowitz D. The Tennessee Mouse Genome Consortium: Identification of ocular mutants. Vis Neurosci. In press 2005.
24. Dalke C, Loster J, Fuchs H, Gailus-Durner V, Soewarto D, Favor J, Neuhauser-Klaus A, Pretsch W, Gekeler F, Shinoda K, Zrenner E, Meitinger T, Hrabe de Angelis M, Graw J. Electroretinography as a screening method for mutations causing retinal dysfunction in mice. Invest Ophthalmol Vis Sci 2004; 45:601-9.
25. Don RH, Cox PT, Wainwright BJ, Baker K, Mattick JS. 'Touchdown' PCR to circumvent spurious priming during gene amplification. Nucleic Acids Res 1991; 19:4008.
26. Jablonski MM, Lu L, Wang X, Chesler EJ, Carps E, Qi S, Gu J, Williams RW. The ldis1 lens mutation in RIIIS/J mice maps to chromosome 8 near cadherin 1. Mol Vis 2004; 10:577-87.
27. Knott SA, Haley CS. Maximum likelihood mapping of quantitative trait loci using full-sib families. Genetics 1992; 132:1211-22.
28. Stockton RA, Slaughter MM. B-wave of the electroretinogram. A reflection of ON bipolar cell activity. J Gen Physiol 1989; 93:101-22.
29. Xu X, Karwoski CJ. Current source density analysis of retinal field potentials. II. Pharmacological analysis of the b-wave and M-wave. J Neurophysiol 1994; 72:96-105.
30. Robson JG, Frishman LJ. Response linearity and kinetics of the cat retina: the bipolar cell component of the dark-adapted electroretinogram. Vis Neurosci 1995; 12:837-50.
31. Kofuji P, Ceelen P, Zahs KR, Surbeck LW, Lester HA, Newman EA. Genetic inactivation of an inwardly rectifying potassium channel (Kir4.1 subunit) in mice: phenotypic impact in retina. J Neurosci 2000; 20:5733-40.
32. Penn RD, Hagins WA. Signal transmission along retinal rods and the origin of the electroretinographic a-wave. Nature 1969; 223:201-4.
33. Robson JG, Frishman LJ. Dissecting the dark-adapted electroretinogram. Doc Ophthalmol 1998-99; 95:187-215.

34. Holbrook JA, Neu-Yilik G, Hentze MW, Kulozik AE. Nonsense-mediated decay approaches the clinic. Nat Genet 2004; 36:801-8.
35. Tantri A, Vrabec TR, Cu-Unjieng A, Frost A, Annesley WH Jr, Donoso LA. X-linked retinoschisis: a clinical and molecular genetic review. Surv Ophthalmol 2004; 49:214-30.
36. Hiriyanna K, Singh-Parikshak R, Bingham EL, Sieving PA. Searching for genotype-phenotype correlations in X-linked juvenile retinoschisis. In: Anderson RE, LaVail MM, Hollyfield JG, editors. New insights into retinal degenerative diseases. Proceedings of the 9th International Symposium on Retinal Degeneration; 2000 Oct 9-14; Durango, CO. New York: Kluwer Academic/Plenum Publishers; 2001. p. 45-53.
37. Hiriyanna KT, Bingham EL, Yashar BM, Ayyagari R, Fishman G, Small KW, Weinberg DV, Weleber RG, Lewis RA, Andreasson S, Richards JE, Sieving PA. Novel mutations in XLRS1 causing retinoschisis, including first evidence of putative leader sequence change. Hum Mutat 1999; 14:423-7.
38. Mashima Y, Shinoda K, Ishida S, Ozawa Y, Kudoh J, Iwata T, Oguchi Y, Shimizu N. Identification of four novel mutations of the XLRS1 gene in Japanese patients with X-linked juvenile retinoschisis. Mutation in brief no. 234. Online. Hum Mutat 1999; 13:338.
39. Shinoda K, Ishida S, Oguchi Y, Mashima Y. Clinical characteristics of 14 japanese patients with X-linked juvenile retinoschisis associated with XLRS1 mutation. Ophthalmic Genet 2000; 21:171-80.
40. Stanga PE, Chong NH, Reck AC, Hardcastle AJ, Holder GE. Optical coherence tomography and electrophysiology in X-linked juvenile retinoschisis associated with a novel mutation in the XLRS1 gene. Retina 2001; 21:78-80.
41. Sato M, Oshika T, Kaji Y, Nose H. Three novel mutations in the X-linked juvenile retinoschisis (XLRS1) gene in 6 Japanese patients, 1 of whom had Turner's syndrome. Ophthalmic Res 2003; 35:295-300.

The print version of this article was created on 27 Jul 2005. This reflects all typographical corrections and errata to the article through that date. Details of any changes may be found in the online version of the article.